NASA/TM-20205000292



Effect of Material Porosity on Residual Stress in an Additive Manufacturing Simulation Using the Generalized Method of Cells

Luis F. Silva and Francisco Yapor Western Michigan University, Kalamazoo, Michigan

Evan J. Pineda Glenn Research Center, Cleveland, Ohio

Peter A. Gustafson Western Michigan University, Kalamazoo, Michigan

NASA STI Program . . . in Profile

Since its founding, NASA has been dedicated to the advancement of aeronautics and space science. The NASA Scientific and Technical Information (STI) Program plays a key part in helping NASA maintain this important role.

The NASA STI Program operates under the auspices of the Agency Chief Information Officer. It collects, organizes, provides for archiving, and disseminates NASA's STI. The NASA STI Program provides access to the NASA Technical Report Server—Registered (NTRS Reg) and NASA Technical Report Server—Public (NTRS) thus providing one of the largest collections of aeronautical and space science STI in the world. Results are published in both non-NASA channels and by NASA in the NASA STI Report Series, which includes the following report types:

- TECHNICAL PUBLICATION. Reports of completed research or a major significant phase of research that present the results of NASA programs and include extensive data or theoretical analysis. Includes compilations of significant scientific and technical data and information deemed to be of continuing reference value. NASA counter-part of peer-reviewed formal professional papers, but has less stringent limitations on manuscript length and extent of graphic presentations.
- TECHNICAL MEMORANDUM. Scientific and technical findings that are preliminary or of specialized interest, e.g., "quick-release" reports, working papers, and bibliographies that contain minimal annotation. Does not contain extensive analysis.

- CONTRACTOR REPORT. Scientific and technical findings by NASA-sponsored contractors and grantees.
- CONFERENCE PUBLICATION. Collected papers from scientific and technical conferences, symposia, seminars, or other meetings sponsored or co-sponsored by NASA.
- SPECIAL PUBLICATION. Scientific, technical, or historical information from NASA programs, projects, and missions, often concerned with subjects having substantial public interest.
- TECHNICAL TRANSLATION. Englishlanguage translations of foreign scientific and technical material pertinent to NASA's mission.

For more information about the NASA STI program, see the following:

- Access the NASA STI program home page at http://www.sti.nasa.gov
- E-mail your question to help@sti.nasa.gov
- Fax your question to the NASA STI Information Desk at 757-864-6500
- Telephone the NASA STI Information Desk at 757-864-9658
- Write to: NASA STI Program Mail Stop 148 NASA Langley Research Center Hampton, VA 23681-2199

NASA/TM-20205000292



Effect of Material Porosity on Residual Stress in an Additive Manufacturing Simulation Using the Generalized Method of Cells

Luis F. Silva and Francisco Yapor Western Michigan University, Kalamazoo, Michigan

Evan J. Pineda Glenn Research Center, Cleveland, Ohio

Peter A. Gustafson Western Michigan University, Kalamazoo, Michigan

National Aeronautics and Space Administration

Glenn Research Center Cleveland, Ohio 44135

Acknowledgments



703-605-6000

Hampton, VA 23681-2199

Effect of Material Porosity on Residual Stress in an Additive Manufacturing Simulation Using the Generalized Method of Cells

Luis F. Silva and Francisco Yapor Western Michigan University Kalamazoo, Michigan 49008

Evan J. Pineda National Aeronautics and Space Administration Glenn Research Center Cleveland, Ohio 44135

> Peter A. Gustafson Western Michigan University Kalamazoo, Michigan 49008

Abstract

The effect of material porosity on final part distortion and residual stresses in a selective laser sintering manufacturing simulation is presented here. A time-dependent thermo-mechanical model is used with the open-source FEA software CalculiX. Effective homogenized material properties for Inconel 625 are precomputed using NASA's Micromechanics Analysis Code with the Generalized Method of Cells. The evolving porosity of the material is estimated with each pass of the laser beam during simulation runtime. A comparison with a homogenous model and the evolving model shows that the model with evolving porosity predicts larger distortions with greater residual stresses.

Nomenclature

ε	sintered porosity
ε_0	initial porosity
ε_{min}	minimum achievable porosity
K	densification coefficient
V_f	volume fraction
S	laser beam penetration depth
η	laser power transmission efficiency
r_0	laser beam radius
v	laser linear speed
l, w	length and width of the laser beam area
ψ	specific energy input
P	nominal laser power
ν	Poisson's ratio
Ε	modulus of elasticity
S_{rr}	stress in xx-direction

 S_{ν} , S_n yield stress, stress at plastic strain n

 U_{xx} displacement in xx-direction

 ε_p plastic strain ρ mass density

k thermal conductivity

h convective heat transfer coefficient

C specific heat capacity

 α coefficient of thermal expansion

Temperature

Introduction

Advancements in additive manufacturing have made it a viable solution for the rapid prototyping and manufacturing of geometrically complex structures. However, the associated part distortion may cause unacceptable dimensional deviations and the accompanying residual stresses can cause premature failure or otherwise weaken the overall structure. These residual stresses occur primarily due to large temperature gradients in powder bed fusion (PDF) additive manufacturing processes such as selective laser sintering (SLS) (Ref. 1). Prediction of these residual fields, optimization of the part and the manufacturing process are desirable.

Powder bed fusion additive manufacturing processes uses a high-powered laser to selectively fuse a metal powder bed, a single layer at a time, into a fully formed part. It is this process of localized material heating and subsequent cooling that induces residual stresses (Ref. 1). Previous literature has indicated that these stresses are linked to a variety of process parameters, including layer thickness and laser beam characteristics (Ref. 2).

Previous physical modeling of the powder bed fusion thermo-mechanical process includes finite element (FE) methods, where a transient thermo-mechanical model is solved (Ref. 3). However, there have been disagreements between these models and experimental results, even after mesh refinements and temperature-dependent material properties were utilized (Ref. 3). Typically, these FE simulations model the material as a homogenous material. Discrete element methods have also been used to account for the heterogeneous nature of the metal powder, simulating an individual or a group of particles and their thermo-mechanical behavior.

The generalized method of cells (GMC) uses a repeating unit cell (RUC) to represent the microstructural domain of a material. Each RUC then contains subcells that are composed of distinct phases (constituent materials in a composite), or in this case, neighboring metal particles and trapped air (pores) in the powder during the sintering process. The material properties and relative dimensions of each subcell can then be used to compute a strain concentration matrix through enforcing traction and displacement continuity conditions. The strain concentration matrix is then used to calculate the effective homogenized macroscopic response (stress/strain, thermal/mechanical material properties) of the RUC (Ref. 4). These effective material properties are used in the constitutive model for the FE simulation, effectively cascading the microstructural response onto the macroscale. GMC can incorporate complex, multi-scaled nonlinear material analysis. The generalized method of cells has the advantage that it can capture the phenomena more natively at the microscale, as opposed to other microstructural to macrostructural estimates, such as the Voigt approximation or the Reuss approximation (Ref. 4, p. 105).

This manuscript estimates the effect of material porosity on residual stresses and residual deformations during the process simulation. In the simulation, the laser pass is modeled as a moving volumetric heat flux. This heat source is used to calculate the evolving material porosity at runtime. The porosity is then used to calculate the effective homogenous material properties using GMC. The properties are tabulated as a function of temperature and porosity for use and interpolation during runtime of a time-dependent thermo-mechanical FE simulation. The effect of the decreasing material porosity from powder to solid is shown to affect the residual stress and deformation fields.

Methodology

Thermomechanical FE Simulation

The additive manufacturing process was simulated using a thermo-mechanical FE model. In this model a transient heat transfer problem is solved for temperature; then, the distribution is applied as a temperature change to a quasistatic structural simulation at every time step. The nonlinearity from temperature-dependent material properties, the temperature-dependent plasticity model, radiation effects in the thermal model, and the changing materials from powder to solid require an iterative solution at every time step. Modeling of liquid phases, the latent heat of a solid to liquid phase change, and any creep effects are neglected. The open-source FE software CalculiX was used to perform the simulations.

External thermal loading was accomplished through a user-defined subroutine in CalculiX. This allows for controlled laser properties such as its path, intensity, and applied heat flux distribution. It has been shown that the laser scanning pattern influences the residual stresses of the final part (Ref. 5). Thus, the open-source 3D slicer software, Slic3r, was used to generate g-code describing the laser path of the part. The laser path produced by Slic3r is intended for a fused deposition modeling (FDM) 3D printing process. It was deemed the path produced was appropriate for this application, since the software is highly configurable and can be set-up with various laser scanning strategies.

A script was written to parse the g-code. It estimates the time required to perform each g-code operation from the laser speed. The script then interpolates the position of the laser at regular time intervals to populate a tabulated file. This file was then read by the user-defined subroutine DFLUX during the runtime in CalculiX. DFLUX determines the laser position from the table and applies a Gaussian distributed volumetric heat flux Q (Ref. 6) as computed by Equation (1) simulating the laser energy input (Ref. 7). Note that, the unitless expression $\pi(1-exp(K_zs))$ is constant in this model at approximately –59.959. The variables x and y are the distances from the beam's center in the respective directions to the integration point, and z is the distance from the top surface to the integration point. The laser center is moved in steps, as described by the tabulated file.

$$Q(x,y,z) = \frac{kK_z \eta P}{\pi \left(1 - \exp\left(K_z s\right)\right)} \exp\left(-kr^2 - K_z z\right)$$

$$r^2 = x^2 + y^2$$

$$K_z = \frac{3}{s}$$
(1)

Element activation simulates the addition of material deposited at every layer. Initially, all the elements of the complete mesh are deactivated and are subsequently reactivated to simulate sintering. A deactivated element is not computed as part of the solver pass. Each layer of elements represents several layers of the additive manufacturing process, as the thickness of an FE element is substantially larger than the thickness of a powder layer. Previous FE simulations, in literature as in Reference 8, have used a

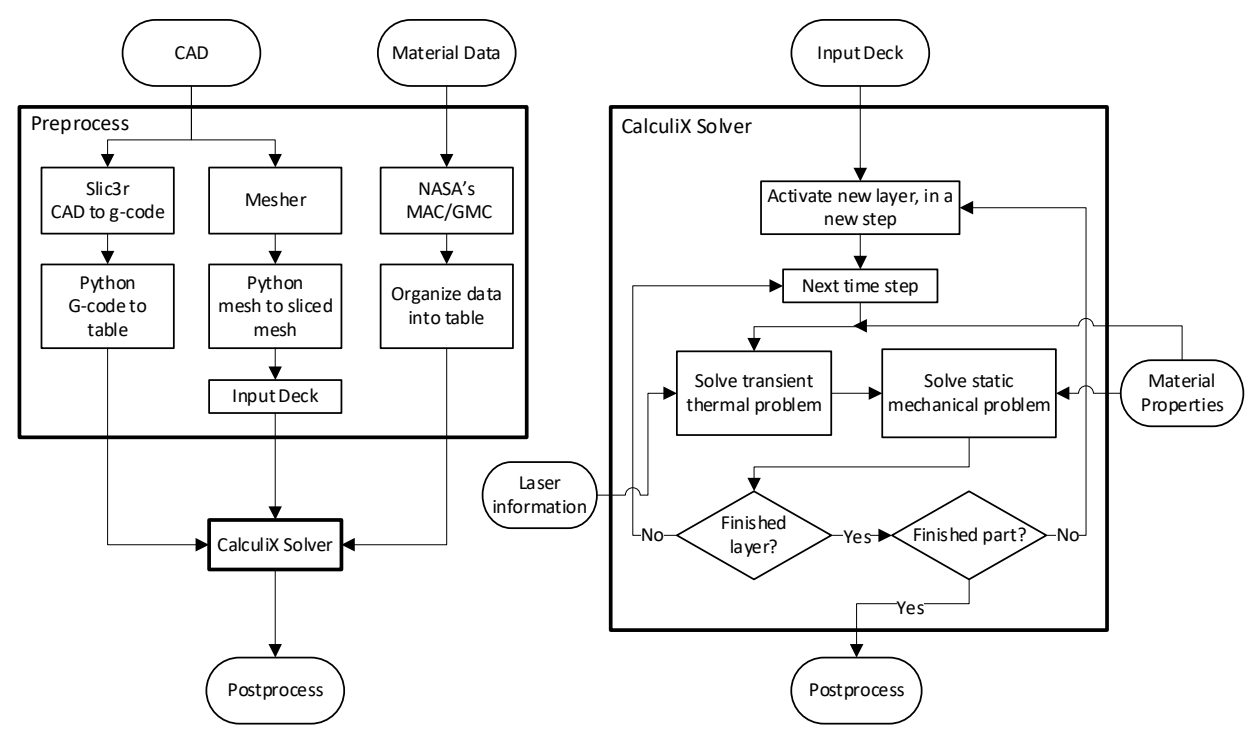


Figure 1.—Implementation flowchart.

couple of elements through the thickness to represent several additive layers. A new layer of elements is added (i.e., activated) after the laser has finished passing through the previous layer. During the activation, since the layer below the newly added elements has already been strained, artificial strain is added to the newly activated elements. This ensures that the newly added, yet deformed element is stress-free. The element layer addition was by predetermined element sets which were grouped in preprocessing. As element topology changes require a new step, the *STEP card was used in the input deck with the *MODEL CHANGE card to perform the addition of the layers. Thus, the input deck is read once, while the laser information and material data (discussed in the next section) are read at every iteration. Figure 1 shows the overall flowchart of the preprocessing and runtime implementation.

At a given time step, each layer of elements contains sintered and powdered material. The distinction is made by the material properties of the integration point. A layer is initialized with powered material properties. During runtime, sintered material properties are assigned once the laser has passed over the integration point. The change in material properties occurs gradually due to its temperature dependence. This is further discussed in the next section.

Locally, mechanical loading is a result of the thermal expansion as calculated in the thermal simulation. The mechanical simulation uses incremental pointwise plasticity as the material constitutive law, assuming isotropic hardening. This was implemented within the user material subroutine by a call to the incremental plasticity subroutine native to CalculiX.

Material Properties

Internal, solution-dependent state variables are used to track the physical state of the material microstructure. Solution-dependent state variables in CalculiX exist for each integration point in the model. Thus, a single element can have different material properties at each of the integration points in a simulation. One solution-dependent state variable is used to store the current predicted porosity of the

material and another to differentiate powder from sintered material. For visualization purposes, a third was used to store the current structural elastic modulus of the material.

CalculiX source codes were modified to allow for a thermal and structural user material capable of altering material properties as determined by interpolating the material properties in a lookup table. A predetermined table of material properties tabulated the material constitutive relationship (elastic modulus, Poisson's ratio, and plastic strain/stress pairs), thermal conductivity, specific heat, and thermal expansion coefficients as a function of temperature, material state (powder or solid) and volume fraction of air to solid (porosity) of the sintered material. This was accomplished by modifying the "materialdata_me.f" and "materialdata_th.f" subroutines in CalculiX to read the properties from the tabulated file and perform a 2D interpolation of the table (once for temperature and again for porosity). If the temperature or porosity being requested was out of bounds from the values specified in the table, the closest temperature or porosity in the table was used (no extrapolations).

The evolution of the porosity of the sintered material ε is predicted during runtime from Equation (2) obtained from Reference 9, where ε_0 is the initial porosity of the powder (assumed here to be 0.3), and ε_{min} is the minimum attainable porosity (assumed here to be 0.0001). The assumptions for the initial and minimum values of porosity are preliminary, used to establish the method. In the future, these properties will be measured. Note that, the densification coefficient K is a function of powder diameter, distribution, and material properties (Ref. 9). Here, it was assumed to be constant at $18.97 \cdot \frac{mm^3}{kJ}$ as a preliminary value, obtained from Reference 9.

The specific energy input ψ is calculated using the laser power P_z , laser linear velocity v, and the laser beam area, characterized by l and w, as shown in Equation (4). The product lw is taken as πr_0^2 . The volume fraction V_f of the sintered material is taken as $V_f = 1 - \varepsilon$, that is $V_f = 1$ represents 100 percent solid and $V_f = 0$ represents 100 percent air. The laser penetration was assumed to exponentially decay into the material as shown in Equation (5), K_z is as defined in Equation (1). It was also assumed that, the estimated porosity ε for an already sintered layer (the layers below the topmost layer) can be used as the initial porosity ε_0 in Equation (3) for subsequent passes of the laser, at each time step. Thus, the porosity of all the layers in the model change during the simulation.

$$ln(1-D) = -K\psi \tag{2}$$

$$D = \frac{\varepsilon - \varepsilon_0}{\varepsilon_{min} - \varepsilon_0} \tag{3}$$

$$\psi = \frac{P_z}{vlw} \tag{4}$$

$$P_z = \eta P exp(-K_z z) \tag{5}$$

Figure 2 shows a simplified illustration of the evolving porosity as the laser passes over the powder. Note that Equation (2) is the empirical approximation to the solution to the underling differential Equation (6), where κ (kappa) is the sintering rate, dependent on the laser specific power. Both equations have been shown to be a reasonable representation to model to the real porosity evolution (Ref. 9).

$$\dot{\varepsilon} = -\kappa \varepsilon \,. \tag{6}$$

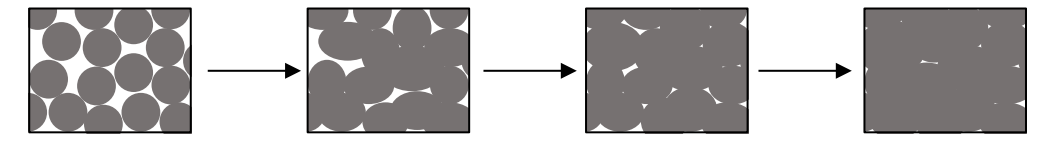


Figure 2.—Evolving Porosity.

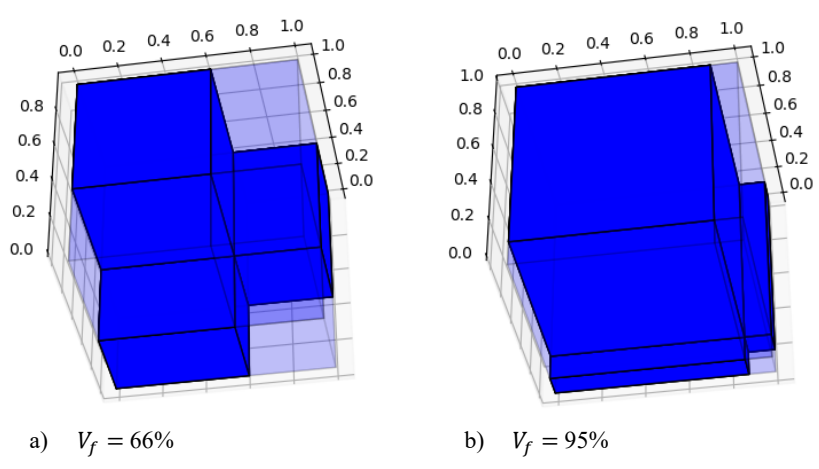


Figure 3.—Open-cell RUC.

The macroscopic homogenized material properties for sintered Inconel 625 were precomputed using NASA's Micromechanical Analysis Code with Generalized Method of Cells (MAC/GMC) for various levels of porosity. A triply periodic open-cell RUC was chosen for the representative arrangement of the partially sintered material, as shown in Figure 3. In the figure, a dark blue rectangular subcell represents a solid material, and a translucent blue represents air. Note that this RUC is assumed to be isotropic, thus there is no need to store any anisotropic material properties.

GMC calculates the material properties in an average sense (Ref. 4). That is, the stress carried by the RUC in a direction is uniformly carried across the subcells. Stress concentrations due to corners are not resolved. Thus, a spherical microstructure would effectively be represented as a rectangular cuboid subcell in GMC.

Properties of Inconel 625 were used for the solid material, as tabulated in Table 1. The mechanical properties of air were estimated as seven orders of magnitude smaller than the mechanical properties of the solid material. The computed sintered material properties are plotted in Figure 4 with respect to temperature at various fractions of solid material. The figure shows that the yield strength and the stress for a given plastic strain decrease as the volume fraction decreases. A similar decrease in those properties can be seen as the temperature increases. All of the material properties computed by MAC/GMC are tabulated in Table 4 in the appendix.

The powdered material properties were set equal to the sintered material properties, except for the modulus of elasticity, at a given temperature and volume fraction. The modulus was estimated to be an order of magnitude smaller than that of the sintered material for a given volume fraction at room temperature. As the temperature of the powder increases, the modulus of the powder was set to linearly increase, until 700 °C, at which the modulus of the powder was made the same to that of the sintered material, at a given volume fraction. This was done to avoid strong C1 discontinuities in material properties and to avoid the strain-softening of the solid Inconel at high strains and temperatures, aiding in numerical convergence. It was assumed that this slow change in powder material properties to sintered

material modulus would not adversely affect the results since the spatial gradient of temperature is extremely high near the laser. Thus, the temperature of the powder material is close to room temperature a small distance away from the laser, and at room temperature, the powder material has a low modulus. These powder material estimates are preliminary and used to establish the methodology. In the future, these properties can be measured and the sensitivity of the results to these properties investigated. Figure 5 shows how this modulus changes with temperature and volume fraction. The solid line represents the linear interpolation used during runtime for temperatures not tabulated.

TABLE 1.—SOLID INCONEL 625 PROPERTIES USED AS A FUNCTION OF TEMPERATURE

A FUNCTION OF TEMPERATURE							
Temperature, °C	20	200	400	700	900		
E GPa	204	193	181	161	145		
υ	0.312	0.303	0.301	0.309	0.284		
$\rho \frac{\text{kg}}{\text{m}^3}$	2700	2700	2700	2700	2700		
k W/m °C	9.8	12.5	15.3	19.8	23.3		
$C \frac{J}{\log {}^{\mathrm{o}}C}$	410	456	511	600	630		
α <u>1</u> °C	12.6E-06	13.1E-6	13.6E-6	15.0E-6	1.60E-05		
S_y MPa	618	610	491	501	195		
$arepsilon_{p,1}$	0.036	0.0782	0.0670	0.1024	0.0535		
S ₁ MPa	727	736	574	689	190		
$arepsilon_{p,2}$	0.092	0.2469	0.1139	0.1584	0.2225		
S₂ MPa	803	876	625	721	167		
$arepsilon_{p,3}$	0.204	0.3030	0.2387	0.4685	0.4908		
S ₃ MPa	902	901	707	601	50		

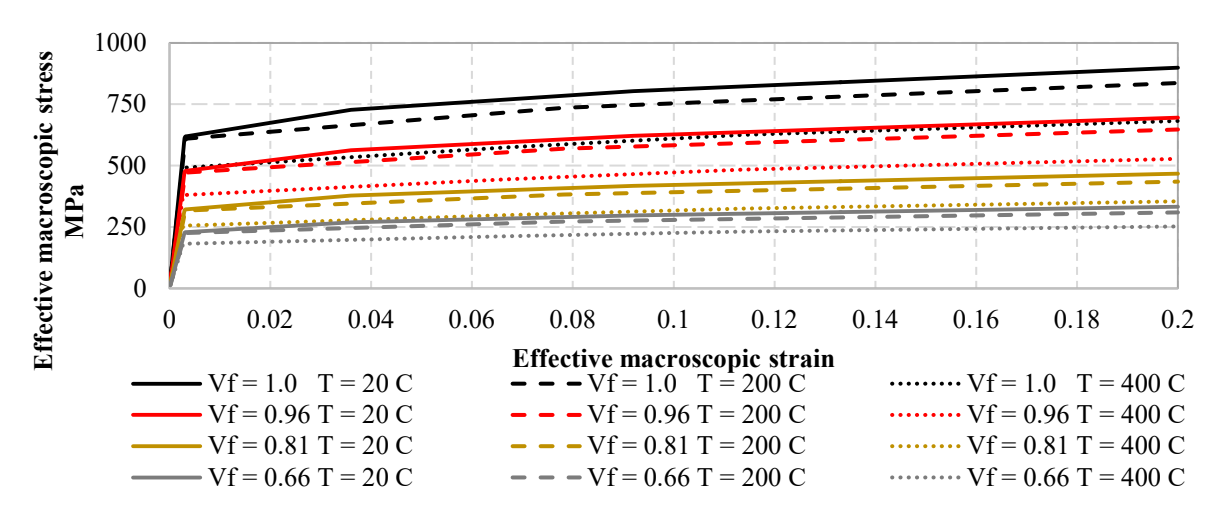


Figure 4.—Sintered material homogenized macroscopic stress-strain curve.

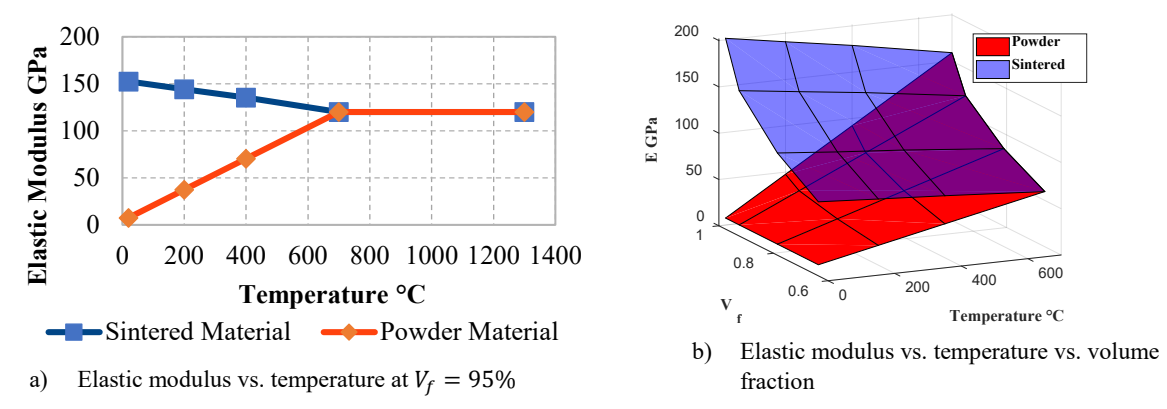


Figure 5.—Elastic modulus vs. temperature vs. volume fraction.

Results

Boundary Conditions

The geometry used, along with the bed and mesh is shown in Figure 6. The dimensions of the printed part are 12 by 12 by 3 mm, while the bed is 9 by 1.5 by 18 mm. The mesh used linear 8-noded hexahedral elements. The bottom of the bed was set to a constant temperature of 70 °C and no displacements were allowed. The elements in the mesh were approximately 1 mm on each side. This allowed the heat flux from the laser beam (with a characteristic radius of 2.5 mm) to be applied to several integration points during a time step. The layer thickness was taken as 1 mm; thus, one element was used through the thickness of a layer.

To avoid the computational cost of modeling the conductive heat flux into a physical region of excess powder, the heat carried away by the powder surrounding the part was modeled as an effective convective heat transfer boundary condition. Here it was assumed that the unmodeled powder changed temperature from its maximum at the surface of the part to its steady-state, far-field temperature within 10 mm. This

gives an effective convective heat transfer coefficient of $h_{eff,powder} = \frac{k}{L} = 362 \frac{W}{m^2 K}$, with an estimated

conductive coefficient of $k_{powder} = 3.62 \frac{W}{mK}$ for the un-sintered powder. The powder thermal conductive

coefficient k_{powder} was estimated from MAC/GMC with a volume fraction of 66 percent. A changing convective boundary condition was applied to the current topmost surface with a convection coefficient of

 $h_{air} = 100 \frac{W}{m^2 K}$. A radiation boundary condition was also applied to the current topmost surface. The

effective emissivity for the radiation was assumed to be 50 percent. The ambient temperature of the air was assumed to be 70 °C. The bed preheat temperature was also set to 70 °C. Figure 7 illustrates these boundary conditions.

Figure 8 shows the scanning pattern used. The laser path was discretized into time steps of 0.05 s for the FE simulation, as shown. The same path was used for all the layers. At a laser speed of 100 mm/s (as shown in Table 2), a layer was scanned in about 5 s. With a dwell time of one second per layer, and twelve layers in the model the total simulated print time is 72 s. A dwell time (time between layers) of 1 s was enough to cool the part to ambient temperature in the simulation. Values used for the laser properties for Equation (1) are listed in Table 2, adopted from Reference 8.

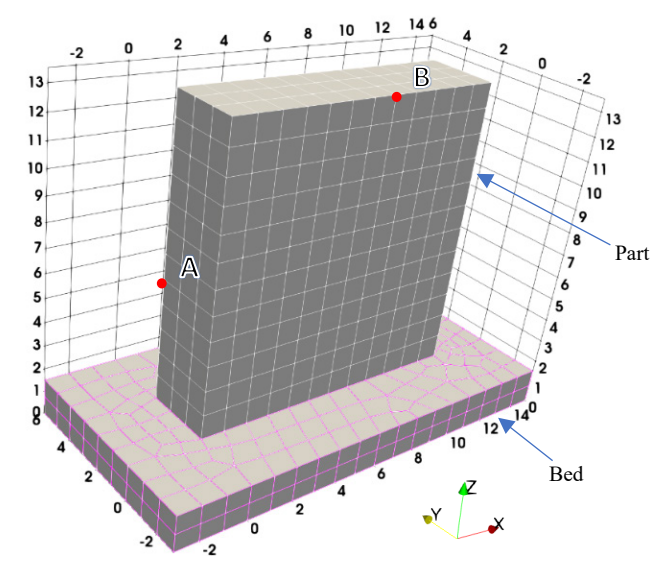


Figure 6.—Geometry and mesh used.

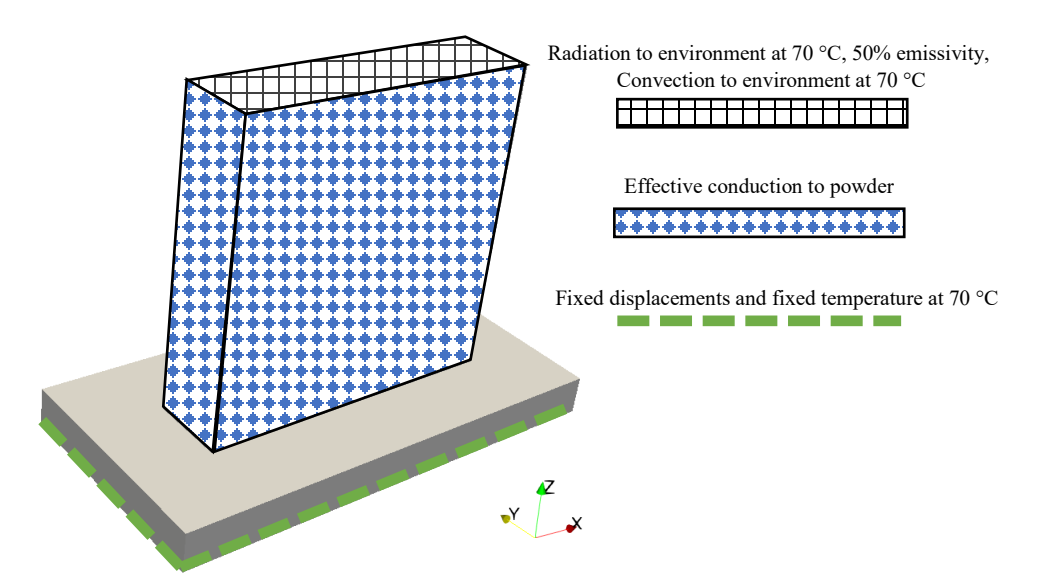


Figure 7.—Boundary conditions applied.

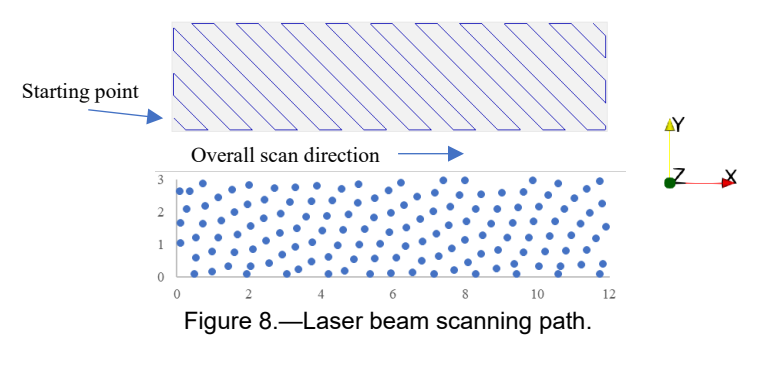


TABLE 2.—LASER PARAMETERS η r_0 mms mmP Wv $\frac{mm}{s}$ 12.512,250100

Evolving Porosity

Post-processing was accomplished with the open-source software ParaView. Figure 9 shows the results of the simulation at the midpoint of part completion. Figure 10 shows the results at the end process after cooling. Corresponding graphs are shown at the same scale.

Figure 11 shows the estimated porosity evolution at a specific node in the model. It shows that the predicted porosity decays from its initial value to its minimum value in approximately a second. The abrupt change in slope in the porosity vs. time plot corresponds with the position of the laser relative to the point in the material.

The stresses in Figure 9 and Figure 10, subplots b, d, and f show that there are primarily compressive residual stresses on the outer surfaces while tensile towards the center. In addition, there are stress concentrations where the part meets the bed, as expected. In addition, the residual stresses in the z-direction are the greatest compared to the other two orthogonal stresses.

The porosity plot in Figure 10 subplot e shows that there is still some porosity at the top surface. This could be due to the laser having passed over the top surface only once. The temperature plot in Figure 9 and Figure 12 subplot c, shows that the temperature is greater inside the part than at the top surface. This temperature gradient may be explained by the convective and radiative boundary conditions on the surface combined with the volumetric heat flux. The temperature dependence of the elastic modulus can also be seen in Figure 9 subplot a.

The deformation in Figure 10, shows that the part swells at the center, with a small amount of deformation towards the top horizontal edges. This behavior also is seen during the simulation of the process, not just after part completion. In addition, the top four corners of the part tend to point in the positive z-direction.

Constant Porosity

A second model with a constant porosity of 10 percent was simulated for comparison. All other parameters including the mesh were kept the same as the previous evolving porosity simulation. Corresponding graphs are shown at the same scale as the previous simulation. The material properties were taken as only dependent on temperature and material state (powder or sintered). Figure 12 and Figure 13 show the results of this simulation.

The elastic modulus plot in Figure 12 subplot a shows that compared to Figure 10 subplot a, the change in the material's modulus from sintered to powder is more severe. This can adversely impact numerical convergence.

Figure 12 and Figure 10 show a similar trend in residual stresses at the end of the printing simulation and similar temperatures during the printing of the part. However, comparing the stresses in the z-direction, the evolving porosity material model tends to show greater stresses in magnitude. Table 3 shows a comparison of residual stresses and distortions, at surface points A and B labeled on the geometry used in Figure 6. Values with a greater magnitude are highlighted for ease. The table shows that the differences in the models can be significant and that the evolving porosity model does not always give greater residual stresses or distortions. The percent increase in magnitude is calculated as:

$$\left(\% \text{ increase in magnitude}\right) = \frac{\left| \text{evolving porosity solution} \right| - \left| \text{contant porosity solution} \right|}{\left| \text{constant porosity solution} \right|} \; .$$

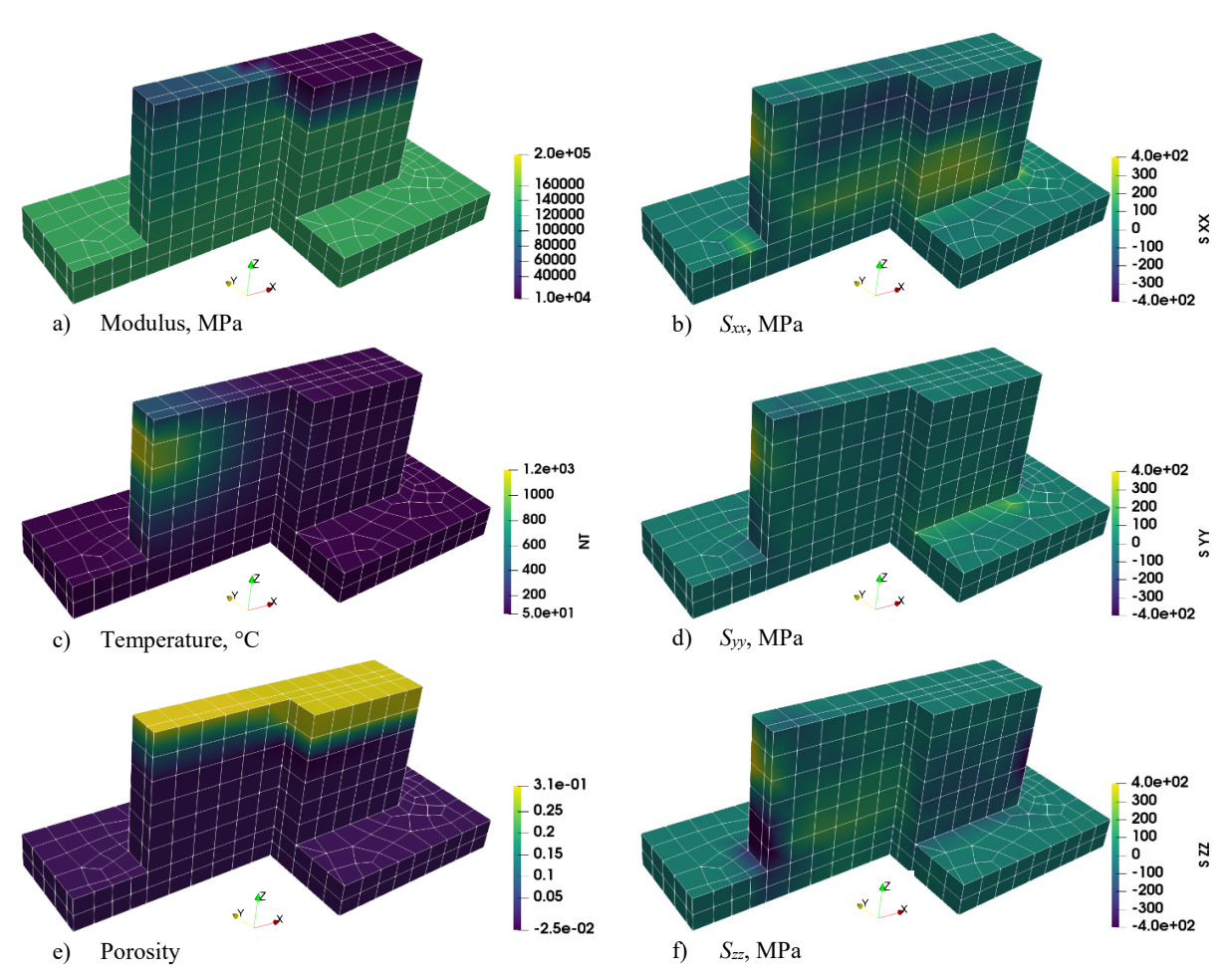


Figure 9.—Results at t = 31.5 s, evolving porosity, no deformation shown.

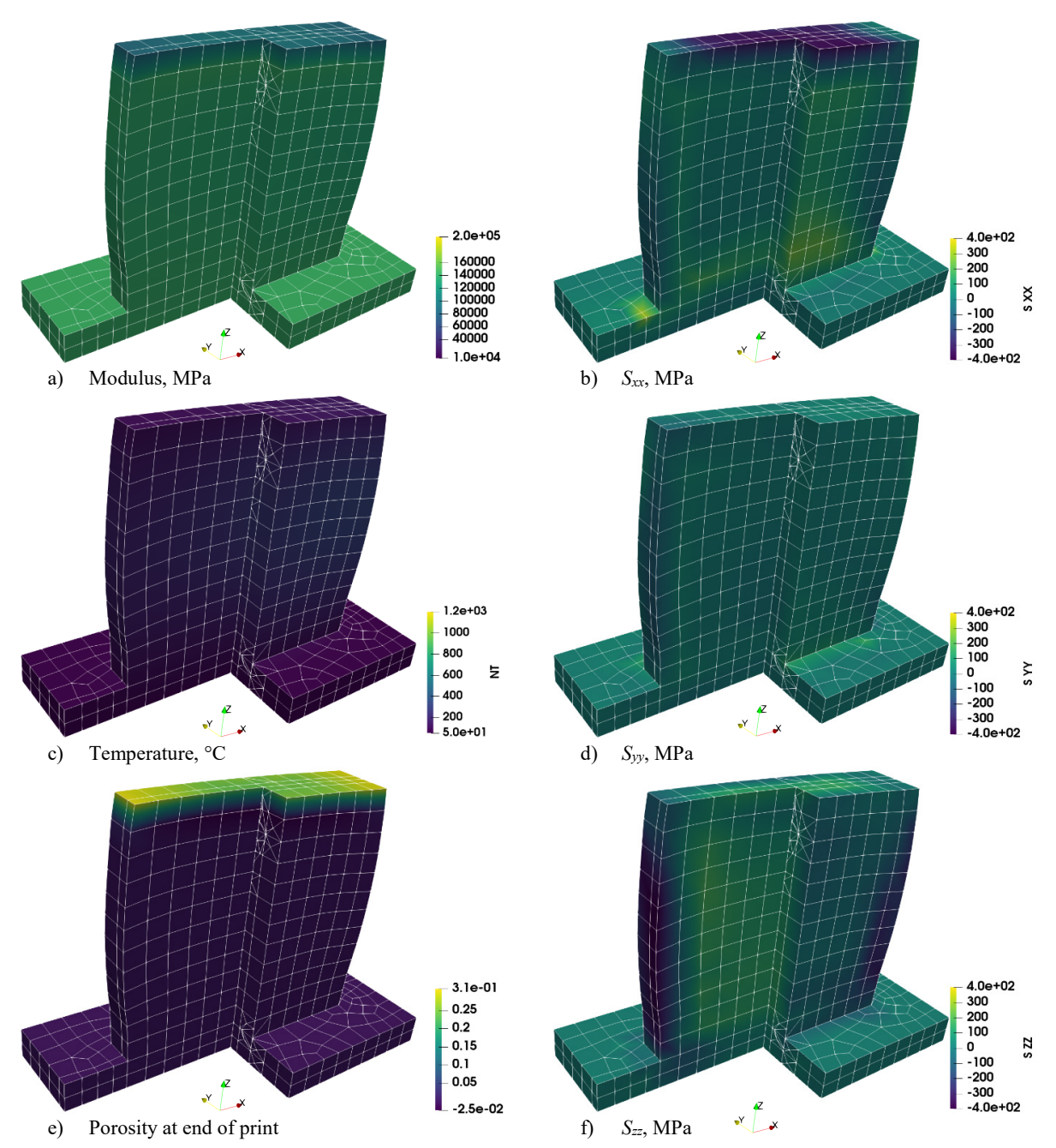


Figure 10.—Results at the end of print, t = 72 s, deformation magnified by 20x, evolving porosity.

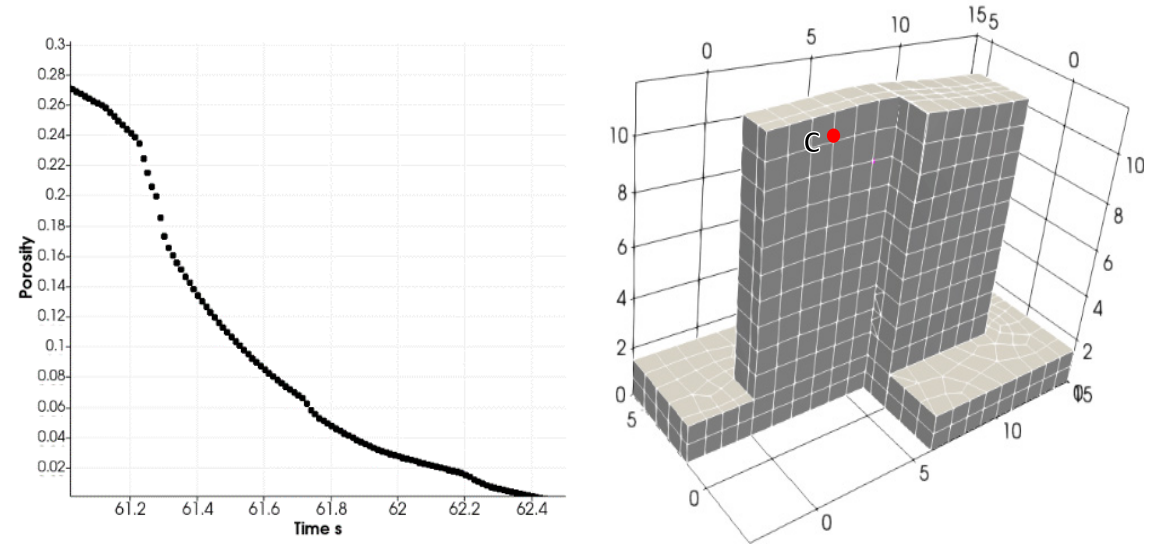


Figure 11.—Estimated porosity vs. time, at node point C.

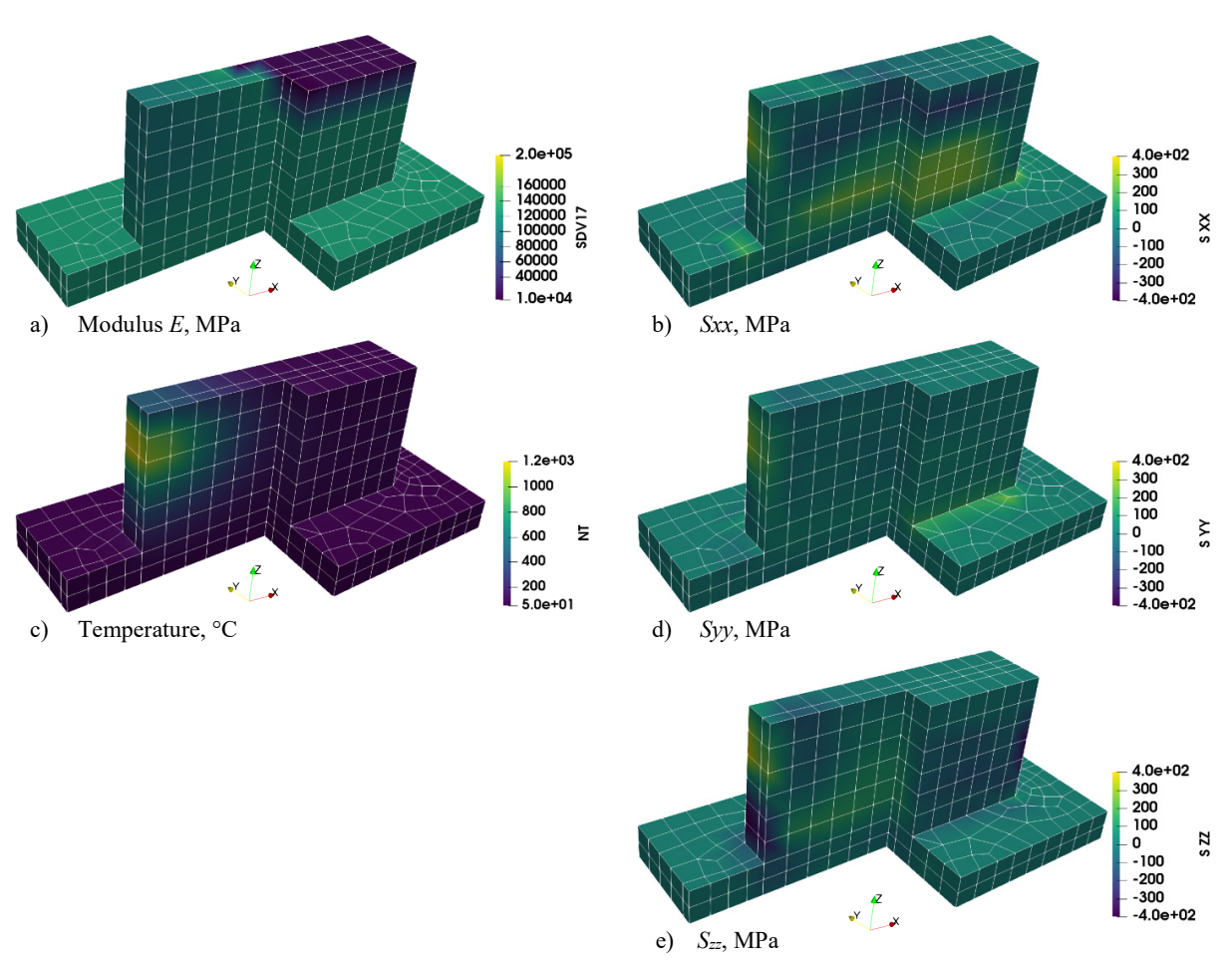


Figure 12.—Results at t = 31.5 s, constant porosity, no deformation shown.

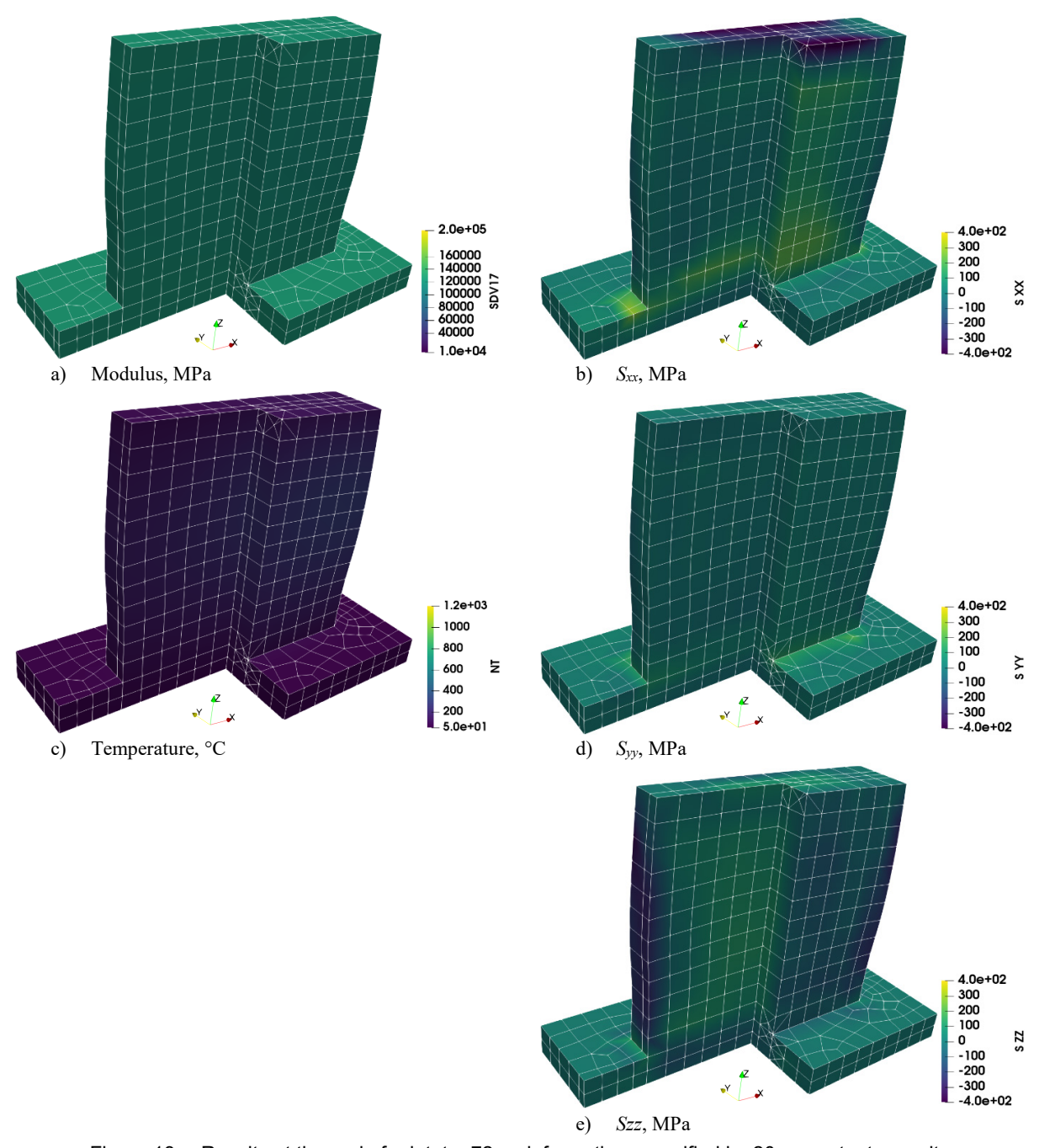


Figure 13.—Results at the end of print, t = 72 s, deformation magnified by 20x, constant porosity.

TABLE 3.—RESIDUAL STRESS AND DISTORTION COMPARISON

	Point A			Point B		
	Constant	Evolving	Percent increase in	Constant	Evolving	Percent increase in
	porosity	porosity	magnitude	porosity	porosity	magnitude
S_{xx} , MPa	-77	-55	-29	-450	-364	-19
Syy, MPa	-60	-16	-73	-11	-1	-91
Szz, MPa	-210	-246	17	-38	-4 7	24
U_{xx} , mm	-0.00894	-0.016807	88	0.001025	0.000541	-47
U_{yy} , mm	0.000809	0.006235	671	0.000174	-8.42e-5	-148
U_{zz} , mm	-0.002287	-0.013365	484	0.002095	0.001269	-39

Discussion

Figure 14 shows a comparison of the Von-Mises stress at the final print time, after cooldown. The figure shows that modeling an evolving porosity results in higher overall residual stresses with larger deformations. The models show a similar stress distribution trend, with evolving porosity model having slightly higher magnitudes. These observations can also be seen comparing the stress plots of Figure 10 and Figure 13. The equivalent plastic strain in the models is compared in Figure 15; again, it shows a similar distribution, but with slightly higher magnitudes. Both models used the same laser parameters, boundary conditions, and mesh.

The peak positive normal stress in the z-direction was calculated at 230 MPa for the evolving porosity model, while the constant porosity model showed a peak positive stress of 145 MPa. The evolving model had a peak displacement of 0.027 mm while the constant model had a peak displacement of 0.016 mm.

This increase in deformation and residual stresses is likely due to the regions with high porosity having to carry the same load (due to thermal strains and constraints by the surrounding material) yet with a lower microscopic cross-sectional area. This reduced cross-sectional area can be seen by comparing the microscopic architectures in Figure 2. The higher applied stresses may result in higher plastic strains, leading to higher residual stresses at part completion and higher part deformation.

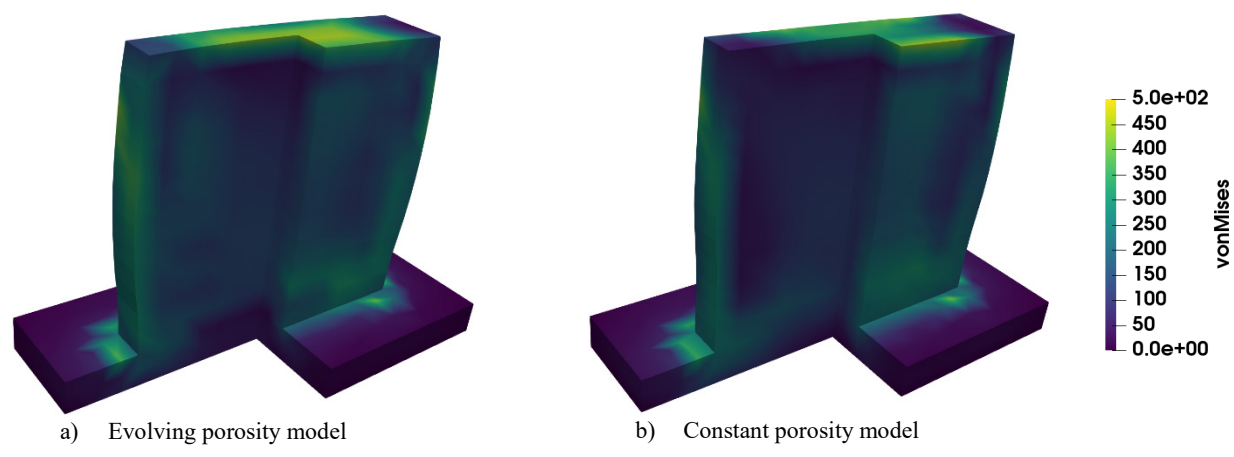


Figure 14.—Von-Mises stress, at t = 72 s, deformation magnified by 20x.

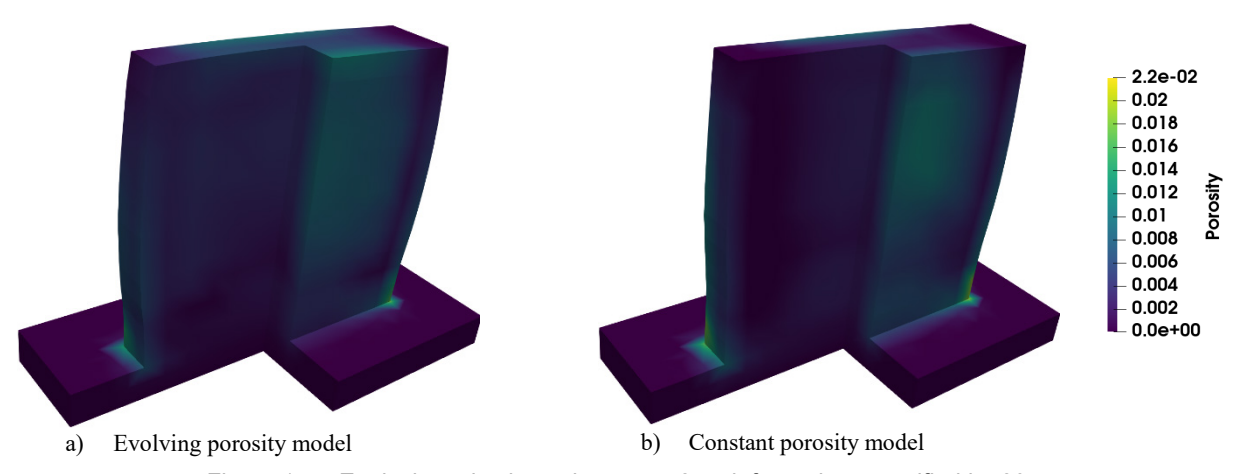


Figure 15.—Equivalent plastic strain, at t = 72 s, deformation magnified by 20x.

A limitation of this work is that to date, no experimental validation has been conducted on the presented work. Several values used have been assumed or approximated (e.g., effective convective heat transfer coefficient). Furthermore, no mesh convergence has been conducted. It is expected that the mesh used here is not able to resolve the fine details in the solution. A model with a refined mesh is currently in progress. In addition, a model with a constant porosity other than the 10 percent used here can be simulated to assess the effects of a different constant porosity. It is speculated that a using a lower constant porosity model will be equivalent to using a material with a higher yield stress, leading to a larger difference between the evolving and constant porosity models. Ongoing work includes the development of validation specimens for experimental validation, and a mesh convergence study.

Conclusion

It has been previously determined that the microstructure evolution and local temperature variation interact mutually (Ref. 9). This paper has used the densification coefficient K, coupled to a time-dependent thermal history, to yield an evolving volume fraction. The volume fraction is used with GMC to provide predictions of temperature and volume fraction dependent stress-strain and plasticity at the micro-scale. These material properties, used in a macro-scale finite element model, compute evolving volume fraction dependent residual stresses. In short, evolving volume fractions impact porosity and consequently impact the residual stresses and deformation.

The work presented here not only provides the capability to simulate the additive manufacturing process, but it may also provide the framework to further couple the macroscale phenomena with more sophisticated microstructural models and constitutive relationships. With this, the influences of the manufacturing parameters (beam scan pattern, speed, dwell times, etc.) on the material properties and residual distortions may also be investigated numerically, supplementing physical experiments. In addition, with the thermomechanical model, it may be possible to investigate the effects of the part geometry on the residual distortions/stresses. Optimization of the geometry to include its manufacturing process is desirable.

Appendix

TABLE 4.—MATERIAL PROPERTIES COMPUTED BY NASA'S MAC/GMC FROM TABLE 1

Material	T °C	V_f	E MPa	υ	$ ho rac{ ext{kg}}{m^3}$	$\frac{k}{w}$		$\alpha \frac{1}{\mathring{c}}$	S _y MP a	$arepsilon_{p,1}$	S ₁ MP a	$arepsilon_{p,2}$	S ₂ MP a
		0.66	7,550	0.190	1,780	3.63	270	1.26E-5	324	0.032	270	0.088	298
	20	0.81	7,550	0.225	2,180	5.10	332	1.26E-5	327	0.032	380	0.088	419
	20	0.95	7,550	0.270	2,560	7.33	389	1.26E-5	469	0.032	546	0.088	602
		0.999	7,550	0.310	2,690	9.69	410	1.26E-5	621	0.032	722	0.088	796
		0.66	21,328	0.184	1,780	4.63	301	1.31E-5	227	0.032	273	0.088	273
	200	0.81	27,707	0.218	2,180	6.50	369	1.31E-5	317	0.075	382	0.244	455
		0.95	37,316	0.262	2,560	6.50	433	1.31E-5	456	0.075	550	0.244	655
Powder		0.999	47,677	0.285	2,630	9.35	456	1.31E-5	540	0.075	652	0.244	776
		0.66	36,637	0.183	1,780	5.67	337	1.36E-5	182	0.111	232	0.236	262
	400	0.81	50,104	0.217	2,180	7.96	414	1.36E-5	256	0.111	325	0.236	368
		0.95	70,389	0.260	2,560	11.44	485	1.36E-5	367	0.111	468	0.236	529
		0.999	92,183	0.299	2,690	15.13	510	1.36E-5	486	0.111	618	0.236	700
		0.66	59,600	0.188	1,780	7.33	383	1.50E-5	186	0.099	255	0.155	267
	700	0.81	83,700	0.223	2,180	10.30	470	1.50E-5	261	0.099	359	0.155	375
		0.95	120,000	0.267	2,560	14.81	551	1.50E-5	375	0.099	516	0.155	540
		0.999	159,142	0.307	2,690	19.58	579	1.50E-5	496	0.099	682	0.155	714
	20	0.66	75,500	0.190	1,780	3.63	270	1.26E-5	324	0.032	270	0.088	298
		0.81	106,000	0.225	2,180	5.10	332	1.26E-5	327	0.032	380	0.088	419
		0.95	152,514	0.270	2,560	7.33	389	1.26E-5	469	0.032	546	0.088	602
		0.999	201,646	0.310	2,690	9.69	410	1.26E-5	621	0.032	722	0.088	796
		0.66	71,400	0.184	1,780	4.63	301	1.31E-5	227	0.032	273	0.088	273
	200	0.81	100,000	0.218	2,180	6.50	369	1.31E-5	317	0.075	382	0.244	455
		0.95	144,290	0.262	2,560	6.50	433	1.31E-5	456	0.075	550	0.244	655
Sintered		0.999	190,773	0.285	2,690	9.35	456	1.31E-5	540	0.075	652	0.244	776
Sintered		0.66	67,000	0.183	1,780	5.67	337	1.36E-5	182	0.111	232	0.236	262
_	400	0.81	94,100	0.217	2,180	7.96	414	1.36E-5	256	0.111	325	0.236	368
		0.95	135,319	0.260	2,560	11.44	485	1.36E-5	367	0.111	468	0.236	529
		0.999	178,911	0.299	2,690	15.13	510	1.36E-5	486	0.111	618	0.236	700
		0.66	59,600	0.188	1,780	7.33	383	1.50E-5	186	0.099	255	0.155	267
	700	0.81	83,700	0.223	2,180	10.30	470	1.50E-5	261	0.099	359	0.155	375
		0.95	120,000	0.267	2,560	14.81	551	1.50E-5	375	0.099	516	0.155	540
		0.999	159,142	0.307	2,690	19.58	579	1.50E-5	496	0.099	682	0.155	714

References

- 1. Mercelis, P., and Kruth, J.P., "Residual stresses in selective laser sintering and selective laser melting," *Rapid Prototyping Journal*, vol. 12, no. 5, p. 254–265, 2006. doi: 10.1108/13552540610707013
- 2. Xing, W., Ouyang, D., Li, N., and Liu, L., "Estimation of Residual Stress in Selective Laser Melting of a Zr-Based Amorphous Alloy," *Materials*, vol. 11, no. 8, 2018. doi:10.3390/ma11081480
- 3. Gobal, A., and Ravani, B., "Physical Modeling of Selective Laser Sintering Process," *Journal of Computing and Information Science in Engineering*, vol. 17, no. 2, 2017. doi: 10.1115/1.4034473
- 4. Aboudi, J., Arnold, S.M., and Bednarcyk, B.A., Micromechanics of composite materials: a generalized multiscale analysis approach, Butterworth-Heinemann, 2013. URL https://books.google.com/books?id=jKJ2VqSwu08C.
- 5. Cheng, Bo, Shrestha, Subin, and Chou, Kevin, "Stress and deformation evaluations of scanning strategy effect in selective laser melting," *Additive Manufacturing*, vol. 12, pp. 240–251, 2016. doi: 10.1016/j.addma.2016.05.007
- 6. Kubiak, M., W. Piekarska, and R. Parkitny, "Theoretical study on thermal and structural phenomena in thin elements heated by a laser beam," *Archives of Mechanics*, vol. 67, no. 1, pp. 3–24, 2015. URL http://search.ebscohost.com/login.aspx?direct=true&db=a9h&AN=100941759.
- 7. Dhondt, G., and Wittig, K., "CalculixX: A Free Software Three-Dimensional Structural Finite Element Program," Web page, 1998. URL http://www.calculix.de/, accessed 2019-12-02.
- 8. Jayanath, S., and A. Achuthan. "A Computationally Efficient Finite Element Framework to Simulate Additive Manufacturing Processes." *Journal of Manufacturing Science and Engineering*, vol. 140, 2018. doi: 10.1115/1.4039092
- 9. Yang, Y., Ragnvaldsen, O., Bai, Y., Yi, M., and Bai-Xiang, "3D non-isothermal phase-field simulation of microstructure evolution during selective laser sintering," *Computational Materials*, 2019. doi: 10.1038/s41524-019-0219-7